

Estimation of the diffusion time in a triaxial galactic potential

P. M. Cincotta * and C. M. Giordano 

Grupo de Caos en Sistemas Hamiltonianos, Facultad de Ciencias Astronómicas y Geofísicas, Universidad Nacional de La Plata and Instituto de Astrofísica de La Plata (CONICET-UNLP), La Plata, B1900FWA, Argentina

Accepted 2023 September 13. Received 2023 September 8; in original form 2023 August 14

ABSTRACT

In this work we apply the Shannon entropy based method to derive a diffusion or instability time in a triaxial model resembling an elliptical galaxy. We succeed in getting an accurate time-scale for diffusion using this novel technique after adopting a particular initial starting space, the one defined by the unperturbed integrals of the system. Comparisons with other standard techniques, such as a least-squares fit on the variance evolution of the integrals and the straight numerical integrations of the equations of motion, are included. The physical results provided in this effort reveal that the role of chaotic motion in triaxial galactic models is almost irrelevant in galactic time-scales, in agreement with previous qualitative approaches to this issue.

Key words: chaos – diffusion – galaxies: kinematics and dynamics.

1 INTRODUCTION

The Solar System as well as almost all the discovered exoplanetary systems are chaotic as it was shown in Laskar (1990), Gayon, Marzari & Scholl (2008), Deck et al. (2012), Barnes et al. (2015), Batygin, Deck & Holman (2015), Gajdoš & Vaňko (2023) among many others.

In Galactic Dynamics, the presence of chaotic motion was already pointed out in the early works of Contopoulos (see Contopoulos 2002 for a collection). Merritt & Friedman (1996), Merritt & Valluri (1996), and Merritt (1999) studied the dynamics of a triaxial elliptical galactic model, focusing on the resonant structure, the orbital families, the chaotic mixing, and the diffusion, while similar issues were addressed in Papaphilippou & Laskar (1998) and Wachlin & Ferraz-Mello (1998). In Bountis, Manos & Antonopoulos (2012), Katsanikas, Patsis & Contopoulos (2013), and Katsanikas & Patsis (2022) the authors investigated the stability analysis of periodic orbits, stickiness phenomena, and diffusion in 3D rotating galactic models.

Though chaos implies exponential divergence of nearby orbits, i.e. a positive maximum Lyapunov exponent, it should be stressed that this locally unstable property does not imply macroscopical instabilities, the so-called stable chaos, first reported in Milani & Nobili (1992) is an illustrative example, also observed in several later works. Thus a relevant issue is whether chaos could lead to large variations of the orbital parameters.

The drift of the unperturbed integrals (or orbital parameters) induced by chaos is known as chaotic diffusion. This instability is easily understood in the framework of near-integrable Hamiltonian systems with more than two degrees of freedom. By near-integrable we mean a system whose Hamiltonian could be written as $H = H_0 + \varepsilon V$, where H_0 is an N -dimensional integrable Hamiltonian with the

full set of independent prime integrals or actions, I_i , $i = 1, \dots, N$, and εV is as small perturbation.

In such a system with $\varepsilon \neq 0$, the unperturbed integrals I_i could change and, within a connected chaotic region of the phase space, the variations could be rather large. The time-scale of the action's drift is known as diffusion time, T_D . On the other hand for $\varepsilon = 0$, the phase space of the system is foliated by invariant tori, the latter being defined by the complete set of integrals, so actions do not change with time and T_D is unbounded.

The diffusion time is a relevant time-scale in real dynamical systems, since it yields the physical time-scale over which the chaotic diffusion could operate erasing the signatures of the initial state of the system.

Any dynamical system has a characteristic time-scale, T_{sys} , thus if $T_D \ll T_{\text{sys}}$, chaos would be effective in driving the system to a nearly stochastic one, while if $T_D > T_{\text{sys}}$, regular motion prevails and chaos becomes irrelevant. In dynamical astronomy, an upper bound to T_{sys} is provided by the Hubble time T_H .

For instance, in Maffione et al. (2015, 2018) it was shown, in a qualitatively way, that only at rather large motion times chaos could be efficient to mix halo orbits in a neighbourhood of the Sun. On the other hand, the literature suggesting an active role of the chaotic diffusion in the dynamical evolution of different planetary systems is huge.

Analytical estimates of T_D could only be obtained for quite small perturbations and therefore they are valid in unrealistic physical models.

Numerical determinations of the diffusion time usually rest on the computation of the variance evolution of the integrals or actions under the assumption of a nearly normal diffusion process, when the action's variance increases almost linearly with time as $\text{Var}(I) \approx 2Dt$, being D the diffusion coefficient and therefore $T_D \sim D^{-1}$. This approach is followed to investigate diffusion processes in quite different dynamical systems, as for instance in Lega, Guzzo & Froeschlé (2003), Froeschlé, Guzzo & Lega (2005), Froeschlé, Lega & Guzzo (2006), Guzzo, Lega & Froeschlé (2005), Lega,

* E-mail: pmc@fcaglp.unlp.edu.ar (PMC); giordano@fcaglp.unlp.edu.ar (CMG)

Froeschlé & Guzzo (2008), Efthymiopoulos & Harsoula (2013), Miguel, Simó & Vieiro (2015), Guillery & Meiss (2017), and Meiss et al. (2018). Estimates obtained through an anomalous diffusion approach, with $\text{Var}(I) \approx 2\bar{D}I^b$, can be found in Kővári et al. (2023) when applied to the dynamics in the trans-Neptunian region of the Solar System.

Alternatively, the diffusion time could be derived from plain numerical simulations, as the required motion time after which chaotic transport operates and drives the motion beyond a given domain of the phase space as it was done in Tsiganis, Varvoglis & Dvorak (2005), Cincotta et al. (2021a, b), Alvez Silva et al. (2021), Cincotta, Giordano & Shevchenko (2022), and Cincotta & Giordano (2023) in planetary dynamics, symplectic maps, and relatively simple Hamiltonian models.

In Cincotta et al. (2019) and Giordano & Cincotta (2018), it was discussed that the assumption of a nearly normal diffusion process is in general not well sustained, at least for moderate motion times. In general the evolution of the variance could be rather noisy and its time evolution could hide any slow secular growth. Nevertheless, it could be improved if, instead of the original action variables, new optimal ones are used. The latter arise from a normal form construction that allows us to eliminate the deformation effect due to oscillations, as for instance it is discussed in Giorgilli (1990), Efthymiopoulos (2012), and Cincotta et al. (2014). On the other hand stickiness effects, that are always present in near-integrable Hamiltonian systems, could prevent the free diffusion leading to anomalous diffusion. In Cincotta & Giordano (2023) the anomalous diffusion is also addressed showing that this alternative approach does not lead to successful results.

Therefore the standard approach of following the variance evolution of the integrals to derive the diffusion coefficient does not yield a good estimate of T_D . In these lines, Giordano & Cincotta (2018) introduced another technique to get the time-scale for diffusion through a Shannon entropy approach. Later on it was successfully applied to different dynamical systems, from relatively simple multidimensional symplectic maps and Hamiltonians to planetary dynamics, as in Cincotta et al. (2021a, b), Alvez Silva et al. (2021), Kővári, Érdi & Sándor (2022), and Cincotta & Giordano (2023).

In this effort we show how to apply the entropy approach to estimate the diffusion time in a triaxial model resembling an elliptical galaxy and compare the obtained results with those derived from the variance evolution and, moreover, with the actual diffusion time arising from the direct numerical integration of the equations of motion.

This work is organized as follows: in Section 2 the entropy formulation is summarized; in Section 3 the triaxial galactic potential model is presented and the appropriate starting space to apply this technique, the angular momentum starting space, is introduced; in Section 4 the diffusion process is discussed as well as the estimation of the diffusion coefficient under different transport laws; in Section 5, the estimations of the diffusion time by means of the entropy approach are presented. Finally, in Section 6 we summarize the main conclusions of this research.

2 THE FORMULATION OF THE SHANNON ENTROPY APPROACH TO DIFFUSION

In this section we summarize the main theoretical results given in Giordano & Cincotta (2018), Cincotta et al. (2021a, b), and Cincotta & Giordano (2023) regarding the Shannon entropy as an efficient technique to estimate the diffusion time in multidimensional dynamical systems. For a global background about the Shannon

entropy theory we refer to Shannon & Weaver (1949), Lesne (2014), and Arnold & Avez (1989).

2.1 The Shannon entropy diffusion coefficient

Let us consider a nearly integrable Hamiltonian dynamical system defined through action angle variables $(I_1, \dots, I_N, \vartheta_1, \dots, \vartheta_N)$, and focus on a given pair of action variables. For example, in a three degrees of freedom autonomous Hamiltonian, since the energy is preserved, the remaining unperturbed integrals would be such a pair of variables, say (I_1, I_2) and consider a given section $\mathcal{S} : \{\vartheta_1 = \vartheta_1^0, \vartheta_2 = \vartheta_2^0\}$. If $N > 3$ the dynamics could be analysed considering suitable pairs of action variables (and their conjugate angles) as it was shown in Cincotta et al. (2021a, b), Alvez Silva et al. (2021), and Kővári et al. (2022).

Setting initial conditions $(I_1(0), I_2(0), \vartheta_1^0, \vartheta_2^0)$ and a motion time T , the corresponding finite orbit γ would intersect $N_s \gg 1$ times the section \mathcal{S} . Let G be the bounded domain of the action plane which includes the N_s crossings.

Introduce then a partition $\alpha = \{\alpha_k, k = 1, \dots, q\}$ on G , i.e. a collection of q disjoint bidimensional cells covering G . Denoting with n_k the number of intersections of γ with \mathcal{S} restricted to the cell α_k , the measure of this element of the partition is $\mathcal{P}(\alpha_k) = n_k/N_s$.

The entropy of γ for the partition α reads

$$S(\gamma, \alpha) = - \sum_{k=1}^q \mathcal{P}(\alpha_k) \ln \mathcal{P}(\alpha_k) = N_s - \frac{1}{N_s} \sum_{k=1}^{q_0} n_k \ln n_k, \quad (1)$$

where $1 \ll q_0 \leq q$ denotes the non-empty elements of the partition. Certainly, the empty elements do not contribute to the sum in (1).

For the adopted partition and any orbit γ , the entropy is always bounded, $0 \leq S(\gamma, \alpha) \leq \ln q_0$, the minimum arises when γ is confined to a single element of the partition, i.e. motion on a torus, while its maximum is reached when all the non-empty elements have the very same measure, $\mathcal{P}(\alpha_k) = 1/q_0$, i.e. ergodic motion.

The last sum in (1) has a simple result when assuming random motion, since n_k follows a Poisson distribution with mean value (and variance) N_s/q_0 , and the entropy for any orbit γ^r reduces to (Cincotta et al. 2021a)

$$S^r(\alpha) \equiv S(\gamma^r, \alpha) \approx \ln q_0 - \frac{q_0}{2N_s}, \quad (2)$$

and thus, under the assumption of $N_s \gg q_0$, the entropy for random motion can be well approximated by

$$S^r(\alpha) \approx \ln q_0. \quad (3)$$

In the case of a strong chaotic trajectory γ , the above approximation partially holds and the entropy of γ results

$$S(\gamma, \alpha) \approx \ln q_0 - \beta \frac{q_0}{2N_s}, \quad (4)$$

where β is a bounded constant close to 1 so $S(\gamma, \alpha) \approx S^r(\alpha) \approx \ln q_0$.

Therefore the time dependence of the entropy for any chaotic orbit $\gamma(t)$ is $S(\gamma(t)) \approx \ln q_0(t)$, being $q_0(t)$ the number of cells visited by γ after a time t .

The time-rate of S over a finite but small time interval $\Delta t \ll T$ reduces to

$$\frac{\Delta S}{\Delta t} \approx \frac{1}{q_0(t)} \frac{\Delta q_0}{\Delta t}. \quad (5)$$

Changes in the number of occupied cells in the interval Δt are caused by the transport process. Assuming that the mean square displacements of the actions in $(t, t + \Delta t)$, $\langle \Delta I_1^2(t) \rangle$, and $\langle \Delta I_2^2(t) \rangle$, yield a measure of $\Delta q_0(t)$, then $\Delta q_0(t) \propto \langle \Delta I_1^2(t) \rangle + \langle \Delta I_2^2(t) \rangle$.

If Σ is the area of G (where the partition of the q cells is defined) then it follows

$$\Delta q_0(t) \approx \frac{q}{\Sigma} (\langle \Delta I_1^2(t) \rangle + \langle \Delta I_2^2(t) \rangle). \quad (6)$$

Assuming a local normal diffusion approximation, the mean square displacement in each direction reads

$$\langle \Delta I_1^2(t) \rangle \approx 2D_t^{(1)} \Delta t, \quad \langle \Delta I_2^2(t) \rangle \approx 2D_t^{(2)} \Delta t, \quad (7)$$

where $D_t^{(i)}$ is a local diffusion coefficient, when the trajectory is restricted to the domain $(I_1(t), I_2(t)) \times (I_1(t + \Delta t), I_2(t + \Delta t))$ and thus

$$\frac{\Delta q_0(t)}{\Delta t} \approx 4 \frac{q}{\Sigma} D_t, \quad D_t = \frac{1}{2} (D_t^{(1)} + D_t^{(2)}). \quad (8)$$

Therefore, from the above derivations, an entropy-like diffusion coefficient in the interval $(t, t + \Delta t)$ can be defined as

$$D_S(\gamma(t)) := \frac{1}{4} \frac{\Sigma}{q} q_0(t) \frac{\Delta S}{\Delta t}(t). \quad (9)$$

If $L = [T/\Delta t]$ is the number of intervals where $D_S(\gamma(t))$ is computed, then a global diffusion coefficient for γ is provided by the average over the L intervals,

$$D_S(\gamma) := \frac{1}{L} \sum_{k=1}^L D_S(\gamma(t_k)) = \langle D_S(\gamma(t_k)) \rangle, \quad (10)$$

and an instability time can be defined as

$$T_{\text{inst}} = K \frac{\Delta^2}{D_S}, \quad (11)$$

where Δ^2 denotes a given mean square displacement, the squared distance between the initial and some boundary values of the actions, K being a numerical factor of the order of 1 that takes into account the anisotropic character of the diffusion.

Even though the entropy depends on the partition, a discussion about a suitable selection is given in Cincotta et al. (2021b) and Cincotta & Giordano (2023). On the other hand, therein it is shown that $D_S(\gamma(t))$ depends on the partition in a quite smooth way and, in the case of a nearly continuous distribution of the n_k , it becomes independent of the partition.

3 THE TRIAXIAL MODEL

In order to illustrate the application of the Shannon entropy approach to a triaxial galactic model, we take the quadrupolar potential introduced in Muzzio, Carpintero & Wachlin (2005)

$$\Phi(\mathbf{r}) = -f_0(\rho_0(r)) - f_x(\rho_x(r))(x^2 - y^2) - f_z(\rho_z(r))(z^2 - y^2), \quad (12)$$

being ρ_j a softened radius defined as $\rho_0^2 = r^2 + \epsilon^2$ while $\rho_x^2 = \rho_y^2 = r^2 + 2\epsilon$, where the softening parameter is set as $\epsilon = 0.01$.

The functions $f_j(\rho_j)$ were derived after frozen an N -body simulation and fitted according to the following laws,

$$f_j = \frac{C_j}{[\rho_j^{k_j} + q_j^{k_j}]^{l_j/k_j}}, \quad j = 0, x, z. \quad (13)$$

where the coefficients are given in Table 1.

Fig. 1 shows the behaviour of the functions f_j 's with r , being $f_z < 0$, $f_0, f_x > 0$, and $f_x > |f_z|$ for all values of r while for $r \gtrsim 0.33$ it is $f_0 > f_x$.

The model reproduces several dynamical properties of elliptical galaxies, such as mass distribution, flattening, triaxiality, and rotation

Table 1. Coefficients of f_j given by equation (13).

j	C_j	k_j	q_j	l_j
0	0.92012657	1.15	0.1340	1.03766579
x	0.08526504	0.97	0.1283	4.61571581
z	-0.05871011	1.05	0.1239	4.42030943

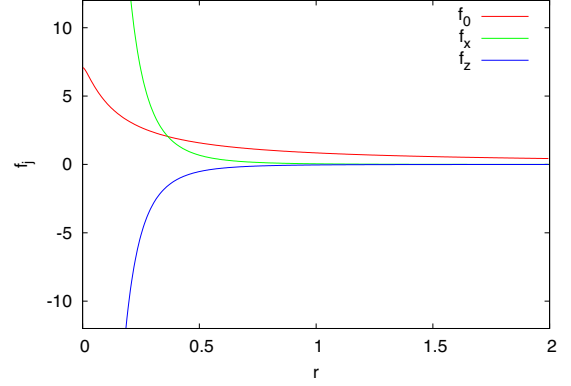


Figure 1. Dependence of the f_j given by equation (13) with r .

(Muzzio 2006). The potential is triaxial with semi-axes X, Y, Z satisfying $X > Y > Z$. The minimum of the potential is $\Phi(0, 0, 0) \approx -7$.

The global dynamics of this model has already been investigated in Cincotta, Giordano & Muzzio (2006) and Maffione et al. (2011), and herein we summarize the main theoretical aspects already discussed in the first one.

If we adopt spherical coordinates (r, θ, ϕ) the potential

$$V(r, \theta, \phi) = \Phi(x(r, \theta, \phi), y(r, \theta, \phi), z(r, \theta)),$$

takes the form

$$V(r, \theta, \phi) = V_0(r) + V_1(r) \cos 2\phi + V_2(r) \cos 2\theta + V_3(r) \cos 2(\theta + \phi) + V_4(r) \cos 2(\theta - \phi), \quad (14)$$

where

$$\begin{aligned} V_0(r) &= -\tilde{f}_0(r) - \frac{1}{4} r^2 \tilde{f}_z(r) < 0, \\ V_1(r) &= -\frac{r^2}{2} \left(\tilde{f}_x(r) + \frac{1}{2} \tilde{f}_z(r) \right) < 0, \\ V_2(r) &= -\frac{3}{4} r^2 \tilde{f}_z(r) = 3(V_0(r) + \tilde{f}_0(r)) > 0, \\ V_3(r) &= V_4(r) = -\frac{1}{2} V_1(r) > 0, \end{aligned} \quad (15)$$

and

$$\tilde{f}_j(r) = f_j(\rho_j(r)); \quad j = 0, x, z.$$

The dependence of the coefficients with respect to V_0 against r is presented in Fig. 2, where it becomes clear that for $r \gtrsim 1$, V_0 dominates the dynamics and thus the system is close to a spherical one.

Due to the smallness of V_j/V_0 , $j = 1, \dots, 3$, the Hamiltonian in spherical variables can be written as a near-integrable one,

$$H(\mathbf{p}, \mathbf{r}) = H_0(\mathbf{p}, \mathbf{r}, \theta) + \mathcal{V}(\mathbf{r}), \quad (16)$$

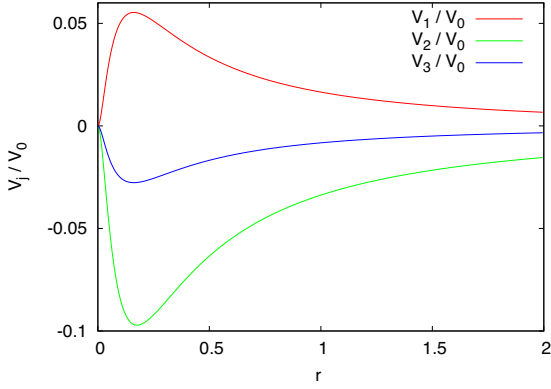


Figure 2. Coefficients of $V(r, \theta, \phi)$ given in (14) relative to $V_0(r)$.

where

$$H_0 = \frac{p_r^2}{2} + \frac{p_\theta^2}{2r^2} + \frac{p_\phi^2}{2r^2 \sin^2 \theta} + V_0(r), \quad (17)$$

and

$$\mathcal{V} = V_1(r) \cos 2\phi + V_2(r) \cos 2\theta + V_3(r) \cos 2(\theta + \phi) + V_4(r) \cos 2(\theta - \phi). \quad (18)$$

Since H_0 is an integrable Hamiltonian, then

$$H_0 = h, \quad L_z = p_\phi, \quad L^2 = p_\theta^2 + p_\phi^2 \csc^2 \theta, \quad (19)$$

are the three unperturbed action-like integrals, while \mathcal{V} could be considered a perturbation. Instead of L^2 as an unperturbed integral we take $L = |L|$.

The above integrals apply in the case of tube families, those that circulate around either the x or z axis.

In Schwarzschild (1993) and Papaphilippou & Laskar (1998) different starting spaces including the most relevant orbital families are introduced, such as the (x, z) space where the remainder variables are set to 0 except for p_y , which results from the energy preservation. In Maffione et al. (2011) the authors provide the global dynamical picture of this model adopting such starting spaces and estimate the amount of chaos using different dynamical indicators and for energies ranging from $h = -0.7$ to $h = -0.1$. For box orbits, that are well displayed in the linear momentum starting space, about 65 per cent of the orbit sample are chaotic while for the tube family, this fraction falls below 20 per cent. Therefore it could be expected that the unstable chaotic motion could play a central role in the dynamics of this system.

3.1 Global dynamics in angular momentum space

Herein we adopt a different approach to display the global dynamics of the model. After fixing the energy, we use the unperturbed integral (L, L_z) starting plane restricted to a given position of the configuration space.

In what follows we adopt $h = -0.5$ and in order to get a time-scale of the model at this energy level, let us mention that the period of the circular orbit leading to the long-axis tube family is about 7 in the given units of the system. A similar period applies for the circular orbit that parents the short-axis tube family.

In all the numerical experiments the integrations were carried out with a Runge–Kutta 7/8th-order integrator, the so-called DOPRI8 routine (Hairer, Norsett & Wanner 1987), Prince & Dormand (1981), where the local tolerance was set to 10^{-15} .

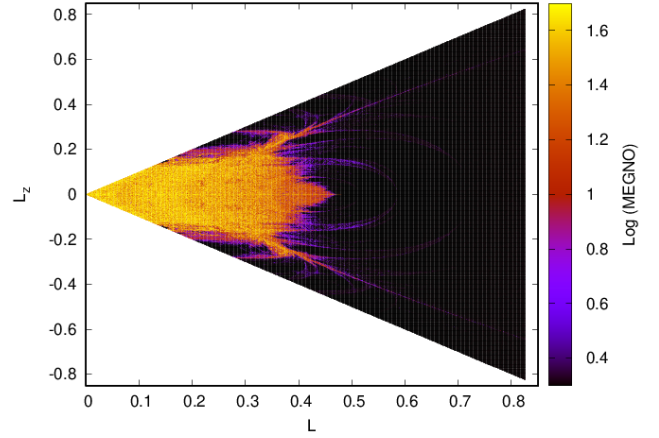


Figure 3. MEGNO contour plot, in logarithmic scale, for $h = -0.5$, $x_0 = 0$, $y_0 = 0.9$, $z_0 = 0$ in the (L, L_z) starting space. The dark colours denote stable and nearly stable motion while dark and light yellow correspond to chaotic and strong chaotic motion (recall that $\log 2 \approx 0.3$).

Fig. 3 displays a contour plot of the MEGNO¹ values computed after a time-span of 1500 time units for a large sample of orbits, the initial conditions being $x_0 = 0$, $y_0 = 0.9$, $z_0 = 0$, $0 \leq L < 0.83$, $-L \leq L_z \leq L$ with a step $\Delta L = \Delta L_z = 10^{-3}$.

The MEGNO is a fast dynamical indicator that provides in an efficient way the maximum Lyapunov exponent (mLE) of an orbit (see Cincotta & Simó 2000; Cincotta, Giordano & Simó 2003; Cincotta & Giordano 2016 for a general description and applications). Its computation requires the integration of both the equations of motion and the first variational ones as for the mLE. For stable motion the MEGNO takes the asymptotic value 2, while for a chaotic orbit with $mLE \mu > 0$, it grows linearly with time as $(\mu/2)t$.

This particular behaviour of the MEGNO with time implies that, for short times, its value allows us to separate regular and chaotic motion and thus the size of the chaotic regions revealed by this indicator is almost independent of the motion time considered. We adopt a comparatively large time-span (1500 units of time) in order to obtain simultaneously confident values of the finite-time mLE computed in the usual way.

In the figure, dark colours denote stable motion (resonant or quasi-periodic), while yellow indicates highly chaotic dynamics. A cut-off value of the indicator was adopted, $MEGNO \leq 100$. As a reference, the largest values of the finite-time mLE are about 0.38 in the most chaotic regions while the smaller ones are close to 6×10^{-3} , consistent with the $\ln t/t$ law for quasi-periodic motion.

Notice that in the region $0 \leq L \lesssim 0.48$ chaotic motion reveals different degrees of dynamical hyperbolicity, while for $L \gtrsim 0.48$, most of the action plane looks like stable. In this starting angular momentum space the short-axis tube orbits (that rotate around the z axis) lie in the narrow strips close to $L_z \approx \pm L$, the separatrix lines set apart the long-axis and the short-axis tube families. Within the long-axis tube family, the separatrix that cross $L_z = 0$ near $L \approx 0.60$ divides the inner and outer ones. Clearly the outer tube orbits appear at large L with $L_z < L$. On the other hand, the box family only shows up around the origin. Some other filamentary structures can be observed in the figure which correspond to resonant motion within the tube families.

¹Mean Exponential Growth factor of Nearby Orbits.

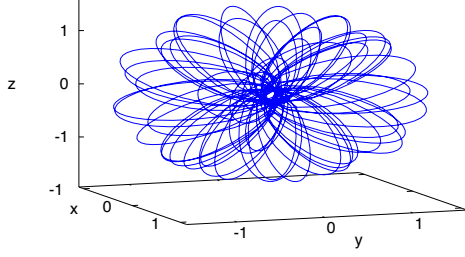


Figure 4. Orbit for initial conditions $h = -0.5$, $x_0 = 0$, $y_0 = 0.9$, $z_0 = 0$, $L = 0.38$, $L_z = 10^{-4}$ after $t = 300$ units of time.

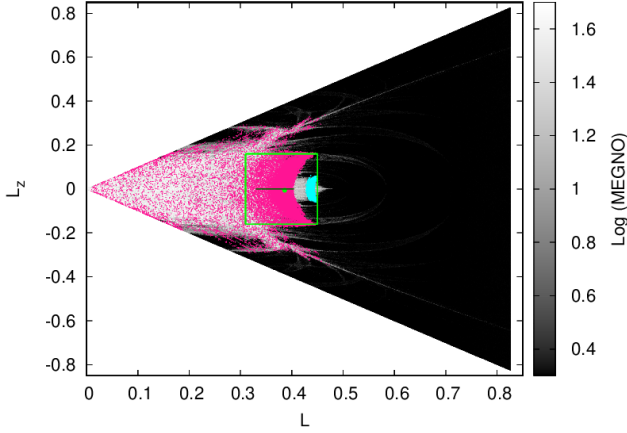


Figure 5. An initial ensemble indicated as a green point at $L = 0.38$, $L_z = 10^{-4}$ is followed onto a MEGNO grey scale contour plot. The concomitant trajectories for the initial ensemble that intersect the section $|x| + |y - 0.9| + |z| < 0.1$ are depicted in magenta. A similar initial ensemble, located at $L = 0.44$, $L_z = 10^{-4}$, is also followed up to $t = 1.5 \times 10^5$ and its crossings with the section are plotted in cyan. The small segment in dark-green at $L_z = 10^{-4}$ with $0.33 \leq L < 0.404$ represents a set of initial conditions adopted for the subsequent experiments regarding the diffusion time, defined as the required time for the motion to leave the window depicted in green (see the text for details).

4 DIFFUSION

Let us investigate the diffusion within the chaotic component of the angular momentum space shown in Fig. 3. To this end, we set again $h = -0.5$, $x_0 = 0$, $y_0 = 0.9$, $z_0 = 0$ and take an ensemble of $n_p = 500$ random initial conditions centred at $L = 0.38$, $L_z = 10^{-4}$, and of size 10^{-6} . The orbit with initial conditions at the centre of the ensemble is represented in Fig. 4 after 300 time units and, while chaotic, it looks like an inner long-axis tube orbit.

Each initial condition in the ensemble is integrated up to 1.5×10^5 time units with a time-step 0.1. Such a small time-step is adopted in order to look for the intersection of the orbits with the slice or section $\mathcal{S} : |x| + |y - 0.9| + |z| < 0.1$.

Fig. 5 shows in magenta the diffusion of the initial ensemble (indicated as a green point) onto a grey scale MEGNO contour plot similar to the one shown in Fig. 3.

Notice that the diffusion spreads over the chaotic component but remains most of the time in the vicinity of the initial ensemble. Nevertheless the region at $0.41 < L < 0.46$, $-0.1 < L_z < 0.1$ is not explored, a barrier seems to prevent the free diffusion over the full chaotic domain. A similar initial ensemble but centred at $L = 0.44$, $L_z = 10^{-4}$ is also followed onto the section \mathcal{S} up to $t = 1.5 \times 10^5$, the corresponding diffusion is shown in cyan in Fig. 5 revealing that, for

the considered motion times, both chaotic regions are not connected. However, further numerical experiments show that only for much larger motion times could both regions be connected, i.e. an example of stickiness phenomena.

4.1 On the nature of the diffusion

In this section, we address some relevant aspects regarding the nature of the diffusion. In a recent work (Kővári et al. 2023), the role of anomalous diffusion in the trans-Neptunian region of the Solar System was discussed. In this work the authors assume that the variance evolution of a given fast action, say I , related with the semi-axis, eccentricity, and inclination elements, evolves following a diffusion-like process such that

$$\text{Var}(I(t)) = 2\tilde{D}_I t^b, \quad (20)$$

where b is known as the Hurst exponent (Hurst 1951) and \tilde{D}_I is a diffusion-like coefficient. Indeed, the dimensions of \tilde{D}_I depends on the exponent b while in the case of $b = 1$, $\tilde{D}_I = D_I$ is the classical diffusion coefficient with its standard dimensions.

Following the above-mentioned work (as well as others like Cincotta et al. 2014), the natural way to characterize the diffusion rests on the relation (20) in logarithmic scale, such that $\log \text{Var}(I(t))$ has a linear dependence on $\log(t)$ with slope b . If $b \approx 1$ the diffusion is normal, while if $b \neq 1$ it is anomalous, $b < 1$ subdiffusion and $b > 1$ superdiffusion.

While theoretically this approach is well sustained, this is not the case from the numerical approach. Let us provide simple examples which help us to illustrate this issue.

Consider the diffusion experiment shown in Fig. 5, corresponding to an initial ensemble centred at $L = 0.38$, $L_z = 10^{-4}$ as well as another similar one but centred at $L = 0.40$, $L_z = 10^{-4}$ (not shown in the figure), where the diffusion is much more confined than in the given example.

Define $J^2 = L^2 + L_z^2$ which encompasses the diffusion in both L and L_z , as usual in the literature. The ensemble variance of J ,

$$\text{Var}(J(t)) = \frac{1}{n_p} \sum_{i=1}^{n_p} (J(t) - J(0))^2 \quad (21)$$

is then computed (the section on the configuration space is not required) after a motion time 10^5 .

We look for the evolution, in logarithmic scale, of $\text{Var}(J(t))$ and determine by a least-squares fit the exponent b and the coefficient \tilde{D} according to the linear relation $\log(\text{Var}(J(t))) = \log(2\tilde{D}_J) + b \log(t)$. In order to reduce any noise introduced by possible oscillations at short times, the fit was done in the interval $[3 \times 10^4, 10^5]$.

The results are unexpected, the exponent yields $b \approx 0.61$ for $L = 0.38$ while $b \approx 0.09$ in the case of $L = 0.40$ revealing a subdiffusive process and the corresponding diffusion-like coefficients are $\tilde{D}_J \approx 4.1 \times 10^{-6}$ and 4.4×10^{-4} , respectively. The errors in all these estimation are less or about 7 per cent. The evolution of the variances and the corresponding fits, restricted to the fitting interval, are shown in Fig. 6. At first glance, the fit follows quite well the variance evolution in logarithmic scale at large times.

On the other hand, if a normal diffusion law is assumed,

$$\text{Var}(J(t)) = 2D_J t + c, \quad (22)$$

where the constant $c \neq 0$ takes into account that the least-squares fit is performed over large motion times, in this case $[10^4, 10^5]$, the fitting values, in linear scale, are $D_J \approx 3.2 \times 10^{-8}$, $c \approx 0.0025$ for $L = 0.38$, and $D_J \approx 1.8 \times 10^{-9}$, $c \approx 0.0021$ for $L = 0.40$, with a maximum

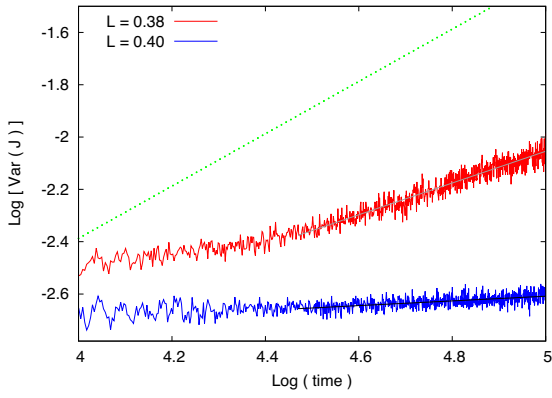


Figure 6. Evolution of the variances $\text{Var}(J(t))$ in logarithmic scale for the ensembles located at $L = 0.38, L_z = 10^{-4}$, and $L = 0.40, L_z = 10^{-4}$. The grey and black lines correspond to the least-squares fit of both variances, $\log(\text{Var}(J(t))) = \log(2\bar{D}_J) + b \log(t)$, with $\bar{D}_J \approx 4.1 \times 10^{-6}, b \approx 0.61$ for $L = 0.38$ while $\bar{D}_J \approx 4.4 \times 10^{-4}, b \approx 0.09$ in case of $L = 0.40$. The dotted green line corresponds to a straight line of unitary slope included for comparison.

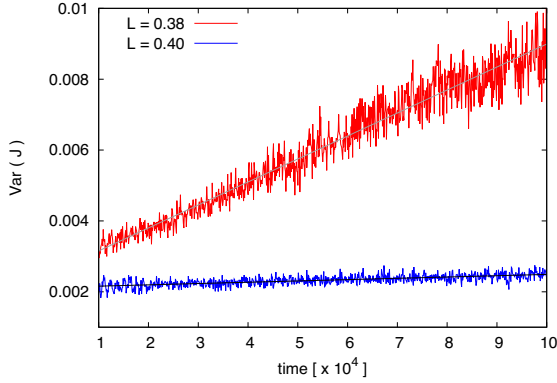


Figure 7. Evolution $\text{Var}(J(t))$ in linear scale for the ensembles at $L = 0.38, L_z = 10^{-4}$ and $L = 0.40, L_z = 10^{-4}$. As in Fig. 6, the black and grey lines correspond to the least-squares fit of $\text{Var}(J(t)) = 2D_J t + c$, with $D_J \approx 3.2 \times 10^{-8}, c \approx 0.0025$ for $L = 0.38$ while $D_J \approx 1.8 \times 10^{-9}, c \approx 0.0021$ in case of $L = 0.40$.

error of about 4 per cent. The results are presented in Fig. 7. As in the previous case, the fit seems to agree with the variance evolution in linear scale.

The results of this section are in some sense awkward, since it is not possible to decide if the diffusion is normal or not, and moreover, what is the value of the macroscopical instability time. In case of the normal assumption, the diffusion time-scale is D_J^{-1} while in the anomalous scenario it is $\bar{D}_J^{-1/b}$. It is simple to check, for the examples given above, that both time-scales differ in several orders of magnitude. Next section will help us to elucidate this point.

5 ENTROPY APPROACH

In order to illustrate the entropy formulation and to compare with the variance approach, let us consider both experiments discussed above. For the same initial ensembles we compute the time evolution of D_S given in (9) for $T = 10^5, \Delta t = 400$, and a partition of $q = 750 \times 750$ equal-sized cells defined in $G = (L_{\min}, L_{\max}) \times (L_{z\min}, L_{z\max}) = (0, 0.83) \times (-0.83, 0.83)$ on \mathcal{S} . The results are almost independent of

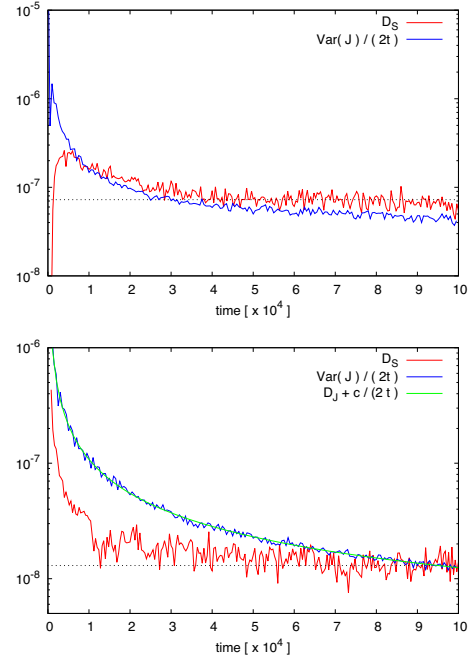


Figure 8. $D_S, \text{Var}(J)/(2t)$ (in logarithmic scale) as a function of time. The top panel corresponds to an initial ensemble located at $L = 0.38, L_z = 10^{-4}$ while the bottom panel to the one at $L = 0.40, L_z = 10^{-4}$. The green curve corresponds to a least-squares fit of the form $\text{Var}(J) = 2D_J t + c$ divided by $2t$ with $D_J \approx 1.84 \times 10^{-9}$ and $c \approx 0.002$.

q provided that it lies in the suitable interval suggested in Cincotta et al. (2021b) and Cincotta & Giordano (2023).

Fig. 8 (top panel) presents the results for the ensemble at $L = 0.38, L_z = 10^{-4}$ where the evolution of D_S is drawn in red. Notice that for $t \approx 4 \times 10^4$ it reaches an asymptotic value close to 7.25×10^{-8} while the ensemble variance of J divided by t , depicted in blue, is still decreasing but at $t = 10^5$ both provide a diffusion coefficient of a comparable order of magnitude. Indeed, the least-squares fit in the normal approximation leads to $D_J \approx 3.2 \times 10^{-8}$, half of the value attained by D_S .

None the less, considering the initial ensemble at $L = 0.40, L_z = 10^{-4}$, the rate of the variance displays a quite different behaviour as Fig. 8 (bottom panel) shows. In this case D_S approaches to a nearly constant value of 1.3×10^{-8} after $t \approx 2 \times 10^4$ while $\text{Var}(J)/(2t)$ decreases as $\sim 1/t$. Using the same least-squares fit as before (for the normal case) for $\text{Var}(J)$, $D_J \approx 1.84 \times 10^{-9}, c \approx 0.002$, the fit of $\text{Var}(J)/(2t)$ is drawn in green. Notice that over the full time-span $c/(2t) \gg D_J$ revealing the nearly $1/t$ law. The computed diffusion coefficients for this experiment differ in one order of magnitude.

In any case, the entropy formulation provides an estimate of the diffusion or instability time despite the nature of the diffusion process. Indeed, for the given examples, D_S converges to asymptotic values at relatively short motion times while, in the variance approach, the results are rather different if a normal or anomalous law for the diffusion is assumed. Although the normal character seems to provide better estimates than the anomalous one, large motion times are required to obtain confident values of D_J . Notice, that in the case of very slow diffusion, D_S is about one order of magnitude larger than D_J .

It remains unclear if $\sim D_S^{-1}$ or $\sim D_J^{-1}$ provide the right diffusion time-scale, issue that will be discussed in the forthcoming section.

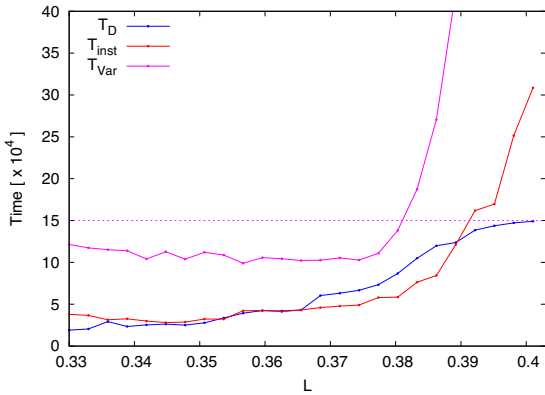


Figure 9. T_D , T_{inst} , and T_{var} against the initial value of L . The dotted line at 1.5×10^5 indicates the total motion time considered in the plain numerical simulations to get T_D .

Let us point out that the main difference between the entropy approach and the normal diffusion approximation over the full time-span rests in equation (7); in the entropy formulation the normal character of the transport process is assumed locally, in each interval Δt . This is in fact the main advantage of the entropy formulation with respect to the variance evolution approach.

5.1 Macroscopical instability times

Now we proceed to investigate the diffusion for several initial ensembles, also of $n_p = 500$, taken along a segment on L . According to the results shown in Fig. 5, we set $0.33 \leq L < 0.404$, $L_z = 10^{-4}$, in order to avoid the quite restricted diffusion corresponding to $L > 0.41$.

First we compute a diffusion time, T_D , through the straight integration of the equations of motion up to $t = 1.5 \times 10^5$. In this experiment, we have defined T_D as the required motion time for the orbits starting at the initial ensemble to cross any of the boundaries $L_1 = 0.31$, $L_2 = 0.45$, $L_{z1} = -0.16$, $L_{z2} = 0.16$ shown in Fig. 5 on the section \mathcal{S} . Actually, in order to reduce stickiness effects, the diffusion time is defined as the average value over the n_p initial conditions in the ensemble.

Later on, the instability time T_{inst} given in (11) is computed for the same set of initial ensembles, with $\Delta = (L_2 - L_1)/2 = 0.07$, $K = 1$, and a motion time $T = 10^5$ with $\Delta t = 400$, so $L = 250$. However as Fig. 8 shows, the average is performed over the last 230 intervals to skip the initial transient. In all the experiments the partition is fixed, the same as the one adopted in the experiments addressed in the previous section.

As an additional estimate, we also derive a diffusion or instability time provided by the variance evolution in the normal approximation, T_{var} , defined in a similar way as T_{inst} in (11),

$$T_{\text{var}} = K \frac{\Delta^2}{D_J}, \quad (23)$$

where D_J is the diffusion coefficient derived from the variance evolution also through a least-squares fit, and K is the same constant as in T_{inst} . For consistency we set $K = 1$ as above.

The results are presented in Fig. 9, T_D in blue, T_{inst} in red, and T_{var} in magenta, as a function of the central value of L in each ensemble.

Recall that the diffusion time presents a saturation value given by the total motion time considered, 1.5×10^5 . Notice however that since T_D is the average over the ensemble, those values of T_D close to

the saturation one reveal that many of the trajectories in the ensemble do not escape. All orbits in ensembles with $L \leq 0.392$ escape, the diffusion time ranging from 2×10^4 up to 1.3×10^5 while for $L > 0.392$ the trajectories remain close to the initial ensemble.

On the other hand, T_{inst} follows a similar trend as T_D , quite close to the latter whenever $L \leq 0.392$ but, for larger values of the angular momentum, it raises up to 3×10^5 revealing that the diffusion is quite slow when $L > 0.392$ and T_{inst} seems to provide the actual value of the diffusion time.

The estimation of the diffusion time given by T_{var} leads to somewhat larger values than T_D in the range $0.33 \leq L < 0.38$, the estimates could be improved if we adopt $K = 1/2$. In this interval T_{var} shows a slight decreasing trend while both, T_D and T_{inst} , exhibit a slow increase with L . For $L > 0.38$, T_{var} takes quite large values in comparison with T_D and T_{inst} .

From these results it turns out that in this triaxial model, the better approximation to the actual diffusion time, i.e. the one obtained through the straight numerical simulations, is provided by the entropy formulation T_{inst} . On the other hand, the variance approach, as already discussed, does not yield confident values of the time-scales for macroscopical instabilities. This conclusion is fully consistent with previous results regarding simple multidimensional dynamical systems of discrete and continuous time as well as different exoplanetary systems (Alvez Silva et al. 2021; Cincotta et al. 2021a, b; Cincotta & Giordano 2023).

From the physical point of view and recalling that the largest estimation of the Hubble time in this model is $T_H \approx 600$ (Muzzio 2006), it becomes clear that diffusion processes are irrelevant since the faster ones require diffusion times larger than 2×10^4 to produce a small change in the unperturbed integrals. This is in accordance with the qualitatively discussion given in Maffione et al. (2015, 2018) regarding the inability of chaotic diffusion to erase the trace of ordered motion in a neighbourhood of the Sun.

While the amount of chaotic motion could be relevant in a given triaxial galactic model, the above results suggest that any macroscopical instability i.e. the chaotic diffusion is almost negligible in the dynamical evolution of, at least, a triaxial galactic model.

6 CONCLUSIONS

In this paper we apply the Shannon entropy approach to derive a diffusion coefficient in a triaxial galactic model. We show that the computed instability times agree quite well with those obtained by a plain numerical simulation that yield the right physical time-scales for a macroscopical instability.

The numerical computation of the Shannon entropy diffusion coefficient does not require the integration of the first variational equations and only involves a counting box scheme while integrating the equations of motion of the system. The computational effort is similar to the one to estimate the diffusion coefficient through the evolution of the action's variances over an ensemble average after performing the appropriate fitting.

The entropy-like diffusion coefficient provides the actual diffusion time when the transport process is slow. Indeed, the one obtained by numerical simulations is always restricted to an upper bound, the total motion time considered. On the other hand, the time-scales obtained by the entropy approach are much more accurate than those from the evolution of the variance in the normal diffusion approximation. If instead, the anomalous regime is assumed, the estimates are quite far from the realistic diffusion times, at least in this particular system.

The results here presented for an autonomous Hamiltonian model resembling an elliptical galaxy reveal once again that the chaotic

diffusion is almost negligible in most galactic systems since the smaller diffusion times are beyond the Hubble time. Therefore, in the line of Binney (see for instance Binney 2018 and references therein) it could be assumed that most of the phase space of a galactic system would be foliated by invariant tori.

ACKNOWLEDGEMENTS

The authors are grateful to Carles Simó for his illuminating discussions and to the reviewer for his valuable comments that allow us to improve this manuscript. PMC and CMG are supported by the Consejo Nacional de Investigaciones Científicas y Técnicas de la República Argentina (CONICET), Project 11220170100569, the Universidad Nacional de La Plata, Project 11G173, and Instituto de Astrofísica de La Plata.

DATA AVAILABILITY

The data underlying this work will be shared on request to the corresponding author.

REFERENCES

- Alves Silva R., Beaugé C., Ferraz-Mello S., Cincotta P. M., Giordano C. M., 2021, *A&A*, 652, A112
- Arnold V., Avez A., 1989, *Ergodic Problems of Classical Mechanics*, 2nd edn. Addison-Wesley, New York
- Barnes R., Deitrick R., Greenberg R., Quinn T. R., Raymond S. N., 2015, *ApJ*, 801, 101
- Batygin K., Deck K. M., Holman M. J., 2015, *AJ*, 149, 167
- Binney J., 2018, *MNRAS*, 474, 2706
- Bountis T., Manos T., Antonopoulos C., 2012, *Celest. Mech. Dyn. Astron.*, 113, 63
- Cincotta P. M., Giordano C. M., 2016, *Lect. Notes Phys.*, 915, 93
- Cincotta P. M., Giordano C. M., 2023, *Phys. Rev. E*, 107, 064101
- Cincotta P. M., Simó C., 2000, *A&AS*, 147, 205
- Cincotta P. M., Giordano C. M., Simó C., 2003, *Phys. D Nonlin. Phenom.*, 182, 151
- Cincotta P. M., Giordano C. M., Muzzio J. C., 2006, *Discrete Contin. Dyn. Syst. B*, 10, 439
- Cincotta P. M., Efthymiopoulos C., Giordano C. M., Mestre M. F., 2014, *Phys. D Nonlin. Phenom.*, 266, 49
- Cincotta P. M., Giordano C. M., Martí J. G., Beaugé C., 2018, *Celest. Mech. Dyn. Astron.*, 130, 7
- Cincotta P. M., Giordano C. M., Alves Silva R., Beaugé C., 2021a, *Phys. D Nonlin. Phenom.*, 417, 132816
- Cincotta P. M., Giordano C. M., Alves Silva R., Beaugé C., 2021b, *Celest. Mech. Dyn. Astron.*, 133, 7
- Cincotta P. M., Giordano C. M., Shevchenko I. I., 2022, *Phys. Rev. E*, 106, 044205
- Contopoulos G., 2002, *Order and Chaos in Dynamical Astronomy*. Springer-Verlag, Berlin
- Deck K. M., Holman M. J., Agol E., Carter J. A., Lissauer J. J., Ragozzine D., Winn J. N., 2012, *ApJ*, 755, L21
- Efthymiopoulos C., 2012, in Cincotta P. M., Giordano C. M., Efthymiopoulos C., eds, *Third La Plata International School on Astronomy and Geophysics: Chaos, Diffusion and Non-integrability in Hamiltonian Systems, Applications to Astronomy*, AAA Workshop Series. La Plata International School on Astronomy and Geophysics, La Plata
- Efthymiopoulos C., Harsoula M., 2013, *Phys. D Nonlin. Phenom.*, 251, 19
- Froeschlé C., Guzzo M., Lega E., 2005, *Celest. Mech. Dyn. Astron.*, 92, 243
- Froeschlé C., Lega E., Guzzo M., 2006, *Celest. Mech. Dyn. Astron.*, 95, 141
- Gajdoš P., Vaňko M., 2023, *MNRAS*, 518, 2068
- Gayon J., Marzari F., Scholl H., 2008, *MNRAS*, 389, L1
- Giordano C. M., Cincotta P. M., 2018, *Celest. Mech. Dyn. Astron.*, 130, 35
- Giorgilli A., 1990, in Benest D., Froeschlé C., eds, *Les Methodes Modernes de la Mecanique Celeste*, Vol. 249. Frontiers, Paris
- Guillery N., Meiss J. D., 2017, *Regular Chaotic Dyn.*, 22, 700
- Guzzo M., Lega E., Froeschlé C., 2005, *Discrete Contin. Dyn. Syst. B*, 5, 687
- Hairer E., Norsett S., Wanner G., 1987, *Solving Ordinary Differential Equations I: Nonstiff Problems*. Springer Verlag, Brelin
- Hurst H. E., 1951, *Trans. Am. Soc. Civil Eng.*, 116, 770
- Katsanikas M., Patsis P. A., 2022, *MNRAS*, 516, 5232
- Katsanikas M., Patsis P. A., Contopoulos G., 2013, *Int. J. Bifurcation Chaos Appl. Sci. Eng.*, 23, 1330005
- Kövári E., Érdi B., Sándor Z., 2022, *MNRAS*, 509, 884
- Kövári E., Forács-Dajka E., Kovács T., Kiss C., Sándor Zs., 2023, *MNRAS*, 524, L26
- Laskar J., 1990, *Icarus*, 88, 266
- Lega E., Guzzo M., Froeschlé C., 2003, *Phys. D Nonlin. Phenom.*, 182, 179
- Lega E., Froeschlé C., Guzzo M., 2008, *Lect. Notes Phys.*, 729, 29
- Lesne A., 2014, *Math. Struct. Comput. Sci.*, 24, e240311
- Maffione N. P., Darriba L. A., Cincotta P. M., Giordano C. M., 2011, *MNRAS*, 429, 2700
- Maffione N. P., Gómez F. A., Cincotta P. M., Giordano C. M., Cooper A. P., O'Shea B. W., 2015, *MNRAS*, 453, 2830
- Maffione N. P. et al., 2018, *MNRAS*, 478, 4052
- Meiss J. D., Miguel N., Simó C., Vieiro A., 2018, *Nonlinearity*, 31, 5615
- Merritt D., 1999, *PASP*, 111, 129
- Merritt D., Fridman T., 1996, *ApJ*, 460, 136
- Merritt D., Valluri M., 1996, *ApJ*, 471, 82
- Miguel N., Simó C., Vieiro A., 2015, *Found. Comput. Math.*, 15, 89
- Milani A., Nobili A. M., 1992, *Nature*, 357, 569
- Muzzio J. C., 2006, *Celest. Mech. Dyn. Astron.*, 96, 85
- Muzzio J. C., Carpintero D. D., Wachlin F. C., 2005, *Celest. Mech. Dyn. Astron.*, 91, 173
- Papaphilippou Y., Laskar J., 1998, *A&A*, 329, 451
- Prince P., Dormand J., 1981, *J. Comp. Appl. Math.*, 7, 67
- Schwarzschild M., 1993, *ApJ*, 409, 563
- Shannon C., Weaver W., 1949, *The Mathematical Theory of Communication*. University of Illinois Press, Champaign, IL
- Tsiganis K., Varvoglis H., Dvorak R., 2005, *Celest. Mech. Dyn. Astron.*, 92, 71
- Wachlin F. C., Ferraz-Mello S., 1998, *MNRAS*, 298, 22

This paper has been typeset from a \LaTeX file prepared by the author.